Combined Approach for Solving the Electromagnetic Induction Imaging Problem

Y Bissessur *
Department of Electrical & Electronic Engineering
Faculty of Engineering
University of Mauritius, Réduit
E-mail: yasdeob@uom.ac.mu

Paper Accepted on 16 June 2008

Abstract

Inverse electromagnetic induction is an imaging technique for reconstructing the conductivity and permeability distributions in a region of interest from measurements of impedance made at its boundary. In general, there are two approaches to the reconstruction problem: the pixel-based approach and the parameter-based approach. This paper describes how both approaches may be combined for a more systematic reconstruction.

Keywords: Electromagnetic induction, inverse problem, image reconstruction.

**For correspondences and reprints*

INTRODUCTION

Non-invasive imaging is an ensemble of techniques for reconstructing the material composition of a region of interest, or object space, from measurements made at its boundary. For example, in electromagnetic induction imaging, it is the magnetic permeability and conductivity contrasts in the object space that are exploited. In this technique, the region of interest is energised by a time-varying magnetic field, usually sinusoidal, which is scattered in regions of high conductivity and reinforced in regions of high magnetic permeability. Measurements of mutual inductance, or impedance, are then made at the accessible boundary of the object space using a sensor array. The change in impedances, relative to an empty object space, is a function of the conductivity and permeability distributions. These measurements are used to reconstruct the object space composition using an appropriate *inversion*, or *image reconstruction*, algorithm. An overview of this technique can be found in (Tapp *et al*, 2003). Applications of electromagnetic imaging include medical imaging (Al Zeibak *et al*, 1993), solidification imaging of molten metals (Xiandong *et al*, 2005; Pham *et al*, 2000), and non-destructive testing of reinforced concrete structures (Gaydecki *et al*, 1994), amongst others. This technique bears strong similarities with microwave imaging (Pastorino, 1998), with the difference that a much lower frequency is used for electromagnetic induction imaging, and this allows for a quasi-static field approximation. The situation presented in this paper is geared towards the imaging of steel reinforcement bars in concrete structures, and is further complicated from the fact that measurements cannot be made over the entire boundary surrounding the region of interest, but only from one side. This form of imaging is also known as planar electromagnetic induction tomography.

An algorithm which has been developed and tested for electromagnetic imaging is the simultaneous increment reconstruction technique (SIRT) (for example, see Bissessur & Peyton, 2006). This algorithm employs a pixel representation of the material distribution, and assumes a linear relationship between the boundary measurements and the material distribution in the object space. In practice, this is not the case since inter-scatter interaction is a nonlinear behaviour. Another form of reconstruction, which is used for general imaging problems, is based on a parametric representation of the object space. These parameters may then be found by an optimisation technique such as the Levenberg-Marquardt algorithm (see Gill *et al*, 1981). A practical example is given in (Isaksen *et al*, 1993) for the shape reconstruction of stratified oil in a circular flow pipe from capacitance measurements made at its boundary. Application of this technique to an electromagnetic inverse problem has been considered by Bissessur & Bhurtun (2005). The success of this technique, however, relies on a proper choice of parameters and their initialisation. In this paper, a systematic approach for the reconstruction problem is presented, which combines the pixel-based and parameter-based algorithms. It is shown how the pixel-based algorithm provides a useful first-order estimate of the object space and, in particular, how the number of objects and object parameters are estimated from an amplitude image. These parameters are then refined by the parametric reconstruction algorithm.

ELECTROMAGNETIC INDUCTION: FORWARD AND INVERSE PROBLEMS

A planar sensor array for electromagnetic induction imaging is shown in Figure 1, in two dimensions. The sensor array consists of 16 coils, which can be energised in turn by a sinusoidal current of frequency 100 kHz, and this produces a time-varying magnetic field over the neighbourhood of the array in the region to be inspected, that is, the object space. This excitation frequency is chosen so that the wavelength is large compared the problem dimensions, and hence a quasi-static field approximation may be employed. The flux linkage with the other sensor coils produces induced voltages at their terminals. The coupling between an excitation and sensor coil can be represented by a mutual-impedance, which can be measured using an impedance analyser. When there are no scattering objects present in the object space, the impedance of coil pairs are referred to as background impedances. These background mutual impedances may be organised in a vector, denoted by $\mathbf{Z}^0$, which consists of 256 complex numbers. For a lossless sensor array, all entries in $\mathbf{Z}^0$ are purely imaginary.

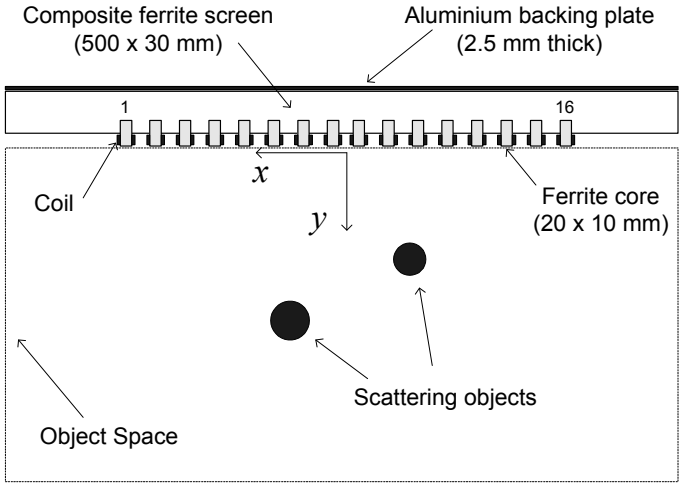

Figure 1. A sensor array for electromagnetic induction imaging

When scattering objects are present in the object space, the magnetic flux linkage between all excitation-sensor coil pair is altered. This results in a change in impedance (from the background value) of every coil-pair in the sensor array. The vector of impedance changes, denoted by $\Delta\mathbf{Z}$, is a function of the size, shape, position, and electrical properties (such as conductivity and magnetic permeability) of the scattering objects. The entries in vector $\Delta\mathbf{Z}$ are, in general, complex numbers. In a practical situation, the material distribution in the object space is unknown, and the *inverse problem* (or *image reconstruction problem*) consists in estimating it from the measurable vector $\Delta\mathbf{Z}$.

Solving the general inverse problem presents a formidable difficulty for several reasons. Firstly, the problem of reconstructing the material distribution $\mathbf{o}(\mathbf{r})$, as a

function of all points **r** in the object space, from a limited number of measurements is underdetermined, or ill-posed. Secondly, the function that relates $\Delta\mathbf{Z}$ to $\mathbf{o}(\mathbf{r})$ is not known explicitly, and numerical and computational methods are normally employed for its evaluation. Thirdly, this function would in general be highly nonlinear, and till date, there is no direct method to invert a general multivariable and multidimensional non-linear function. For these reasons, it is necessary to reduce the number of unknowns, and assume certain *a priori* information.

Electromagnetic scattering inverse problems are generally divided into two categories: *inverse medium problem* and *inverse obstacle problem* (Colton & Kress, 1998). In the former, the unknown is the material distribution as a continuous function of spatial coordinates over the object space. In the latter, the scatterers are considered as compact objects of uniform material composition, which is known. The unknown is the boundary between the scatterers and the host medium (which is assumed to be non-conducting and non-magnetic). The second class of problems are in general much simpler to solve since a fewer number of parameters are needed to specify a boundary than to specify a continuous variation over an entire object space.

In this paper, it is assumed that the object space consists of an unknown number of circular obstacles, denoted by N_c. Furthermore, the centre-position (x_c, y_c) and radius R of the scatterers are unknown, whereas the electrical properties of all scatterers are the same, and known values. It is assumed that scattering objects have conductivity $\sigma = 2\times10^6\,\Omega^{-1}\mathrm{m}^{-1}$ and relative permeability $\mu_R = 600$, which corresponds to the material properties of steel commonly used as reinforcement bars in concrete structures. In other words, the object space material distribution is characterised by an open set of parameters $\boldsymbol{\beta} = \{x_{c1}, y_{c1}, R_1, x_{c2}, y_{c2}, R_2, \ldots\}$.

In the above context, the *forward problem* is defined as the evaluation of $\Delta\mathbf{Z}$ for a known vector $\boldsymbol{\beta}$. An efficient approach for solving this problem is described in (Bissessur & Peyton, 2006). For a compact obstacle, the scattered electromagnetic field is adequately represented by a surface current density and a magnetic dipole density on the surface of the object (Colton & Kress, 1998). In the current problem, the object space is modelled by a two-dimensional compact support $\Re$ in the *x*-*y* plane, representing a cut through a three-dimensional region by the sensor-array plane. Therefore, three-dimensional bars are modelled by circular contours *C* in the *x*-*y* plane. Furthermore, it is assumed that the total electric field is in the *z*-direction, whereas the magnetic field has no *z*-component. Hence the surface current density on a scatterer is defined on *C* and oriented in the *z*-direction, whereas magnetic dipole distribution is defined over the same support but always tangential to *C*. The scattered electric field is then expressed as a sum of the electric field produced by surface current density and a magnetic dipole density, and its *z*-component is given by:

$$E_z(\mathbf{r}) = \oint_C J_S(\mathbf{r}')G_{A1}(\mathbf{r},\mathbf{r}')dC + \oint_C \frac{Z_S}{j\omega\mu_0} J_S(\mathbf{r}')G_{A2}(\mathbf{r},\mathbf{r}')dC \qquad (\mathbf{r} \notin C)$$

(1)

where:

$G_{A1}(\mathbf{r},\mathbf{r}')$ represents the electric field at **r** produced by an impulse current at **r**' and oriented in the *z*-direction, and is given by $\frac{j\omega\mu_0}{2\pi}\ln|\mathbf{r}-\mathbf{r}'|$

$G_{A2}(\mathbf{r},\mathbf{r}')$ represents the electric field at **r** produced by an impulse magnetic dipole at **r**' and oriented in the tangential direction on *C*, and is equal to $\frac{\partial G_{A1}(\mathbf{r},\mathbf{r}')}{\partial \mathbf{n}(\mathbf{r}')}$, with $\mathbf{n}(\mathbf{r}')$ being the outward unit normal on *C* at $\mathbf{r}'$

$J_S(\mathbf{r}')$ is the surface current density at point $\mathbf{r}' \in C$,

Z_S is the surface impedance of the scatterer,

ω is the angular excitation frequency,

and μ_0 is the permeability of free space.

In equation (1), the integrals are evaluated with respect to the coordinates $\mathbf{r}' \in C$. The first integral is referred to as a single layer potential and is continuous across boundary *C*. The second integral is referred to as a double layer potential and is discontinuous across the boundary, and the discontinuity amounts to $\pm\frac{1}{2}Z_S J_S$. Using the superposition principle (Colton & Kress, 1998), and using the fact that the total electric field is zero inside the obstacle, the unknown density J_S in equation (1) may solved for a known incident electric field.

Once, the surface current density on each scatterer has been solved, the change in self-impedance of any coil *i* excited with current *I* can be found from the following relation:

$$\Delta Z = -\frac{1}{I^2}\oint_C \left[Z_S H_t^{(0)} - E^{(0)}\right] J_S \, dC$$

(2)

where $H_t^{(0)}$ and $E^{(0)}$ are the background tangential magnetic field intensity and electric field strength respectively. Equation (2) has been obtained by applying reciprocity relations (Auld *et al*, 1984), and its derivation is given in (Bissessur & Peyton, 2006). For mutual impedance changes ΔZ_{ij}, the background fields $E^{(0)}$ and $H_t^{(0)}$ are taken for the case when coil *i* is energised, whereas the surface current density J_S is calculated from the background field originating from coil *j*. However, due to reciprocity, it would make no difference whether the two field patterns are interchanged. Furthermore, if there is more than one scatterer, each will contribute to a change in impedance and all contributions must be summed.

The impedance change of all excitation-sensor coil pairs are computed using equation (2) and organised in the measurement vector $\Delta\mathbf{Z}$.

For a numerical implementation of equations (1) and (2), the surface of each conductor is discretised as a number of source and observation points. The method of moments may then be used to convert the integral equations into linear algebraic equations. Details of the computational method are outside the scope of this paper and the reader is invited to refer to the paper (Bissessur & Peyton, 2006). The main concern of this paper is on the inverse problem.

The following sections describe how the inverse problem may be solved. For practical reasons, the image reconstruction is not based directly on $\Delta\mathbf{Z}$, but rather on the fractional change in impedance from background, denoted by $\mathbf{\Omega}$, where $\Omega_{ij} = \Delta Z_{ij} / \mathrm{Im}(Z_{ij}^0)$. Two approaches are presented for the inverse problem: a *pixel-based* approach and a *parametric* approach.

A PIXEL-BASED APPROACH TO SOLVE THE INVERSE PROBLEM

In a pixel-based approach to reconstruct the object space, the latter is limited to the region $\Re = \{(x, y) : -16 \le x \le 16\,\mathrm{cm},\ 0 \le y \le 20\,\mathrm{cm}\}$, which is digitised as a uniform grid with a resolution of 1 cm without considering points on the borders. The grid is composed of 31x19 points i.e. 589 pixels altogether. When a circular test object of radius 1 cm, say, is positioned with its centre at a point on the grid, the fractional change in impedances that would result on the sensor array are computed are described in the previous section. It is assumed that the test object behaves as a perfect scatterer and the surface impedance is set to zero. Therefore, the impedance changes corresponding to the test object are purely imaginary, and are converted to purely real by applying the $-j$ operator. The vector of fractional impedance changes calculated for each grid position is the sensitivity of the sensor array for a test object at that location. By sweeping the test object over the entire grid, it is possible to generate an ensemble of sensitivity vectors for the sensor array over region $\Re$. These vectors are then organised as the columns of a *sensitivity matrix*, denoted by **A**, which can be used to construct a linear model of the forward problem. The object function over region $\Re$ may be represented by a vector **f**, where each entry f_i is a complex number representing the material properties at the given grid location (x_i, y_i). For the simplest linearisation of the forward problem, a commonly used approximation for the function $\mathbf{\Omega}(\mathbf{o}(\mathbf{r}))$ is in the following form:

$$\mathbf{\Omega}(\mathbf{f}) = j\mathbf{A}\mathbf{f} \tag{3}$$

For a vector of measured fractional impedance changes $\mathbf{\Omega}_{meas}$, the inverse problem consists in finding **f** such that the product $j\mathbf{A}\mathbf{f}$ is as close as possible to $\mathbf{\Omega}_{meas}$ in the least square sense. An iterative inversion algorithm, such as the simultaneous increment reconstruction technique (SIRT), may be used to solve for

the best-fit image vector **f**. For convenience, we let $-j\boldsymbol{\Omega}_{meas} = \mathbf{p} + j\mathbf{q}$ and $\mathbf{f} = \mathbf{g} + j\mathbf{h}$, so that the real and imaginary image vectors **g** and **h** may be reconstructed from **p** and **q** respectively. First the reconstruction of the real image **g** from **p** is considered. The algorithm starts with an initialised value for **g** say $\mathbf{g}^{(0)}$, which is often taken as the null vector. The corresponding error at iteration *n* is calculated according to:

$$\mathbf{e}^{(n)} = \mathbf{A}\mathbf{g}^{(n)} - \mathbf{p} \tag{4}$$

The object space distribution **f** is then updated according to:

$$\mathbf{g}^{(n+1)} = \mathbf{g}^{(n)} - \lambda \mathbf{S}\mathbf{e}^{(n)} \tag{5}$$

where λ is a small relaxation constant, $\mathbf{g}^{(n+1)}$ is the updated object space to be used in the next iteration, and **S** is another sensitivity matrix constructed as follows. Each row of the matrix **S**, denoted by $\mathbf{s}_i$, is obtained by dividing each column of **A** by its norm squared, that is:

$$\mathbf{s}_i = \frac{\mathbf{a}_i^T}{\left\| \mathbf{a}_i^T \right\|^2} \tag{6}$$

These steps are repeated until a pre-set limit is reached or the errors are sufficiently small. A measure of the data fitting error, such as an error-to-signal ratio (ESR), may be computed after the n^{th} iteration as follows:

$$ESR \ (\text{in dB}) = 10 \times \log_{10} \frac{energy\ of\ \mathbf{e}}{energy\ of\ \mathbf{p}} \tag{7}$$

where the energy of a vector is the sum of the squared values in the vector.

An improvement of the standard SIRT algorithm is given in (Bissessur *et al*, 2004). Initially, the relaxation factor is set to some value, say 0.01. If the error energy $\|\mathbf{e}\|^2$ for the current iteration is less than that of the previous iteration, then the relaxation factor is increased by, say, 10 percent. Otherwise the relaxation factor is decreased to say a quarter of its previous value. This allows the algorithm to track the maximum value that may be used for the relaxation factor at each iteration. A faster convergence is achieved with this modification than with the standard SIRT algorithm, and only about 500 iterations are sufficient to approach very close to the minimum achievable value of ESR with a linear model.

The above algorithm is repeated for the imaginary component of the image, **h**, which is reconstructed from vector **q**. Hence in equations (4), (5) and (7), **g** and **p** are substituted by **h** and **q** respectively. Furthermore, in order to improve the quality of the reconstructed images, constraints may be applied on the pixels at each iteration, depending on *a priori* information available. For example, since the vector **q** is attributed to restive loss, the reconstructed vector **h** may be constrained to all positive pixels at each iteration. However, the vector **g** can have positive or

negative pixel values, depending on whether the scattering object is cancelling or reinforcing the magnetic field on its boundary. If it is known that the object is a strong scatterer, all pixel values in **g** may be constrained to positive values.

A PARAMETRIC APPROACH TO SOLVE THE INVERSE PROBLEM

In a parametric approach to solve the inverse problem, a number N_c of conductors is assumed, and the object space is represented by the set of parameters $\boldsymbol{\beta} = \{x_1, y_1, R_1, \ldots, x_{N_c}, y_{N_c}, R_{N_c}\}$. The inverse problem may then be regarded as finding the vector $\boldsymbol{\beta}_{opt}$ that maximises the resemblance between $\boldsymbol{\Omega}(\boldsymbol{\beta})$ and the measured vector $\boldsymbol{\Omega}_{meas}$. In the Euclidean sense, this is the same as minimising the cost function ζ, where:

$$\zeta = \|\mathbf{e}\|^2 \tag{8}$$

and **e** is the error vector given by:

$$\mathbf{e} = \boldsymbol{\Omega}(\boldsymbol{\beta}) - \boldsymbol{\Omega}_{meas} \tag{9}$$

The minimisation of the cost function may be done by a deterministic method employing the standard Levenberg-Marquardt algorithm, or a variant form, as described below. The algorithm starts with an estimate $\boldsymbol{\beta}^{(0)}$ of the object space. The forward problem is solved with this estimate, and the partial derivatives of $\boldsymbol{\Omega}$ with respect to each entry in $\boldsymbol{\beta}$ are also estimated from a finite-difference method, as follows:

$$\frac{\partial \boldsymbol{\Omega}(\boldsymbol{\beta})}{\partial \beta_m} \approx \frac{\boldsymbol{\Omega}(\boldsymbol{\beta} + \Delta\beta_m) - \boldsymbol{\Omega}(\boldsymbol{\beta})}{\Delta\beta_m} \tag{10}$$

where $\Delta\beta_m$ represents a small perturbation on the particular object space parameter. The partial derivatives may be organised in the form of a Jacobian matrix **J**, where each column is computed according to equation (10). In the standard LM algorithm, the change $\Delta\boldsymbol{\beta}$ that should be made on the vector $\boldsymbol{\beta}^{(0)}$ is obtained by solving the following equation:

$$\left(\mathbf{J}^T\mathbf{J} + \lambda\mathbf{I}\right)\Delta\boldsymbol{\beta} = -\mathbf{J}^T\mathbf{e} \tag{11}$$

where **I** is the identity matrix, $\mathbf{J}^T$ is the conjugate-transpose of **J**, and λ is a small regularisation parameter to ensure that the matrix on the right-hand side is reasonably well-conditioned. The choice of λ is in fact a compromise and based on trial and error. A very small λ may lead to a faster convergence towards the solution $\boldsymbol{\beta}_{opt}$, but there is also a high risk of divergence outside the region of

interest. On the other hand, a larger λ gives more stability but a slower convergence.

A systematic procedure to obtain a proper regularisation parameter λ was proposed by Ciric *et al* (1997). The algorithm starts with an initial value of λ according to the following:

$$\lambda^{(0)} = \frac{1}{N_\beta} tr(\mathbf{J}^T \mathbf{J}) \tag{12}$$

where N_β is the number of entries in $\boldsymbol{\beta}$. At each iteration, the current value of $\lambda^{(n)}$ is used to calculate $\Delta\boldsymbol{\beta}$ according to equation (11). If this results in a decrease in the cost function then the regularisation parameter is decreased by a factor, say by 0.5 times. Otherwise the parameter is increased by a factor, say 1.5. This means starting with a sufficiently large regularisation parameter to avoid divergence, and gradually decreasing it to gain to convergence rate. Equation (11) may therefore be written in the following form:

$$\Delta\boldsymbol{\beta} = -\left(\mathbf{J}^T \mathbf{J} + \frac{\rho}{N_\beta} tr(\mathbf{J}^T \mathbf{J})\, \mathbf{I} \right)^{-1} \mathbf{J}^T \mathbf{e} \tag{13}$$

Here, a normalised regularisation parameter ρ is introduced. Its value is initialised to 1, and updated at each iteration in the same way as before. In order to assess the correctness of a solution, the cost function may be used as a measure of performance, which may also be expressed in decibels as in equation (7).

Once that $\Delta\boldsymbol{\beta}$ has been calculated using equation (13), the object space vector may then be updated as follows:

$$\boldsymbol{\beta}^{(n+1)} = \boldsymbol{\beta}^{(n)} + \Delta\boldsymbol{\beta} \tag{14}$$

The updated object space is then used in another iteration. This process is repeated until the reconstructed parameters are sufficiently close to the actual values, or if the data-fitting error has converged to a minimum.

A COMBINED APPROACH TO SOLVE THE INVERSE PROBLEM

In the previous sections, two approaches to solve the inverse problem were presented. In the first, a linear model of the scattering problem is assumed and no initial information of the object space is required. A complex image $\mathbf{f}$ is reconstructed from which information may be extracted. In the second approach the objects are represented parametrically. The modelling of the scattering problem is thus more accurate. However, the best-fit function is highly nonlinear and it is necessary to have a good initial estimate of the vector of parameters, $\boldsymbol{\beta}$. In this section, it is shown how the two approaches are combined.

First, a pixel-based reconstruction is attempted since it requires no *a priori* knowledge of the object space. From the reconstructed complex image **f**, an amplitude image **m** may be extracted as follows:

$$m_i = \sqrt{g_i^2 + h_i^2} \tag{15}$$

This amplitude image is then reorganised as a two-dimensional array and displayed as an intensity plot. This plot will reveal the presence of objects in the object space and is used to extract as much information as possible on the object space. First, the number of objects is estimated by inspection of the image for groups of pixel with high intensity. A rectangular window, W, is then defined for each distinct group of pixel. The centre (x_c, y_c) of the object is estimated by calculating the centre of moment over the window, as follows:

$$x_c = \frac{\sum_{i \in W} m_i x_i}{\sum_{i \in W} m_i} \qquad y_c = \frac{\sum_{i \in W} m_i y_i}{\sum_{i \in W} m_i} \tag{16}$$

It is also found that the relative area of the object, A_{rel}, can be estimated by summing all the amplitude values over the window, as follows:

$$A_{rel} = \sum_{i \in W} m_i \tag{17}$$

The relative area refers to the ratio of the actual object area and the area of the test scatterer that was used to construct the sensitivity matrix **A**. Since a test object of 1cm radius was used, the radius of a scattering object is estimated by taking the square-root of the relative area. With the estimates (x_c, y_c) and R for each scatterer, the object space vector $\boldsymbol{\beta}$ may be initialised and then refined within a few iterations of the optimisation algorithm. The efficiency of this combined approach is demonstrated in the examples below.

RESULTS

Example 1

Consider a large circular scatterer of radius 6cm and centred at (0, 9)cm in the object space. The forward problem is solved with these values and a vector $\boldsymbol{\Omega}$ of 256 values is obtained, representing the fractional impedance change of each excitation-sensor coil pair. The object space is first reconstructed from $\boldsymbol{\Omega}$ using the adaptive SIRT algorithm with 500 iterations. Both real and imaginary parts of the reconstructed image are constrained to positive pixel values. The combined amplitude image **m** is shown in Figure 2(a). This image reveals a single object over the rectangular window with corners (-4, 4)cm and (4, 12)cm. The centre of moment is calculated as (0.0, 8.2)cm, and the sum of amplitudes over this window gives a relative area of 20.7, corresponding to an estimated radius of 4.6cm. In the second phase of the reconstruction, the object space parameters are initialised to

{0.0,8.2,4.6}cm and a nonlinear reconstruction is attempted. The iterative scheme is terminated when the reconstructed object parameters are within 1mm of the actual values. After only 6 iterations, the object parameters converge to {0.0, 9.0, 6.0}cm, as shown in Figure 2(b).

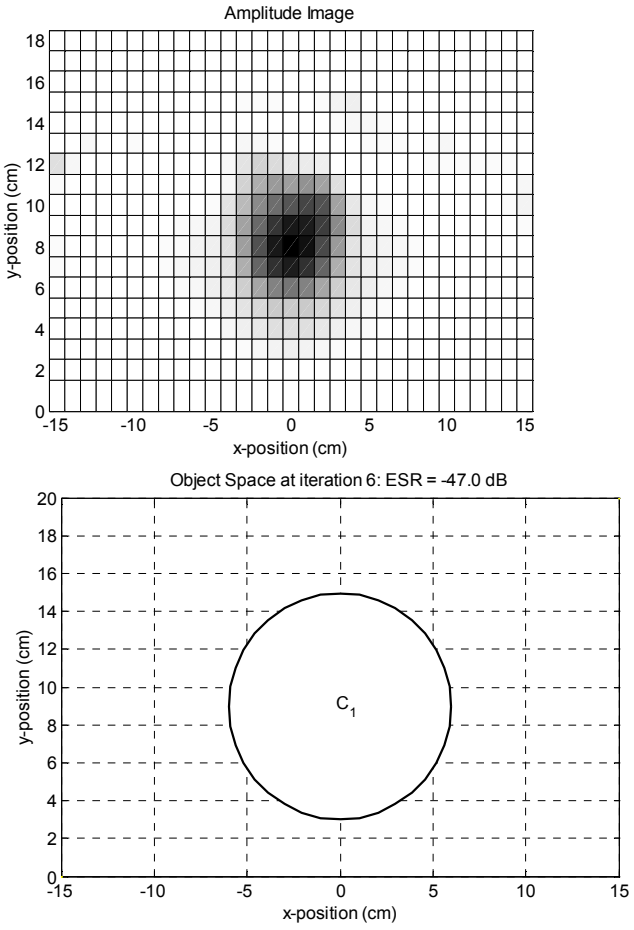

(a) (b)

Figure 2: (a) Amplitude image and (b) parametrically reconstructed object for Example 1.

Example 2

Now consider a small circular scatterer of radius 0.3cm and centred at (0, 6)cm in the object space. After solving for the measurement vector $\boldsymbol{\Omega}$, the object space is first reconstructed using the adaptive SIRT algorithm. This time, it is necessary to constrain the real image to negative pixel values and the imaginary part to positive pixel values. The combined amplitude image is shown in Figure 3(a). The image reveals a single object over the rectangular window with corners (-3, 4)cm and (3, 8)cm. The centre of moment is calculated as (0.0, 6.1)cm, and the sum of amplitudes over this window gives a relative area of 0.08, corresponding to an estimated radius of 0.26cm. In the second phase of the reconstruction, the object space parameters are initialised to with these parameters and a nonlinear

reconstruction is attempted. After 8 iterations, the object parameters have converged to {0.0, 6.0, 0.3}cm, as shown in Figure 3(b).

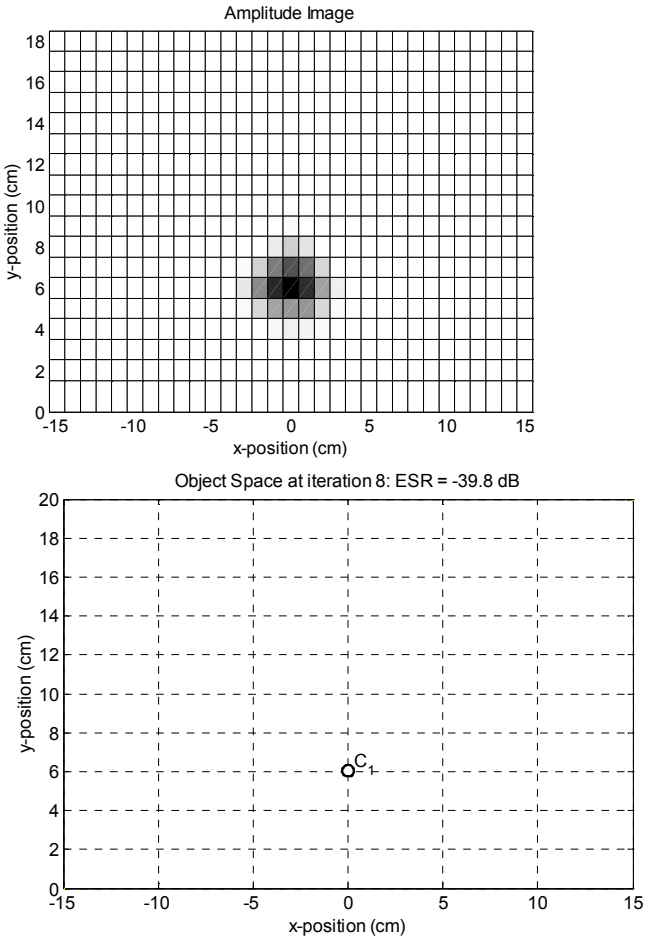

(a) (b)

Figure 3: (a) Amplitude image and (b) parametrically reconstructed object for Example 2.

Example 3

We now consider the reconstruction of two objects of radius 8mm in the object space. The objects are centred at positions (-3, 6)cm and (3, 6)cm. The objects are close enough for their interaction to be significant. The pixel-based reconstruction gives a sufficiently clear image after 1200 iterations, as shown in Figure 4(a). The amplitude image suggests the presence of two objects over non-overlapping windows, the first with corners (-5, 4)cm and (0, 8)cm, and the other with corners (1, 4)cm and (5, 8)cm. The centre of moment of the windows are calculated as (-2.5, 6.2)cm and (2.8, 6.1)cm respectively. The relative areas are found to be 0.40 and 0.36, corresponding to radii of 0.63cm and 0.60cm respectively. These values are then used to initiate the parametric reconstruction scheme. After 9 iterations, the object parameters are correctly estimated within 1mm of the actual values, as shown in Figure 4(b).

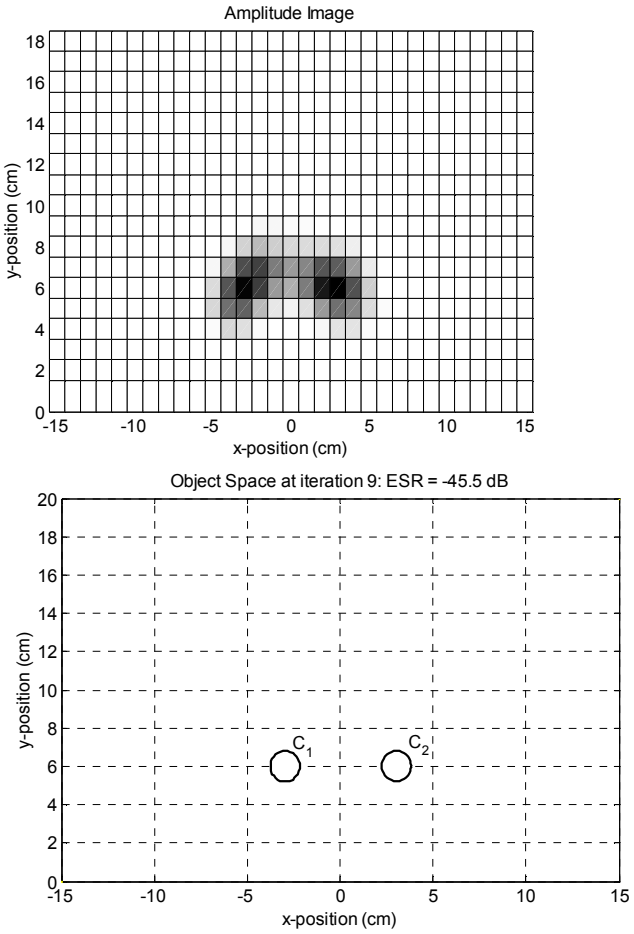

(a) (b)

Figure 4: (a) Amplitude image and (b) parametrically reconstructed object for Example 3.

In all the above examples, the vector $\boldsymbol{\Omega}$ has been generated by simulation, that is, by solving the forward problem for a known set of object space parameters. Therefore, it has been possible to obtain very accurate reconstruction, within 1mm of actual values, after only a few iterations of the parametric algorithm. However in a practical situation, the measurements are corrupted by errors from several sources. However, it is still possible to apply the combined approach to produce a fairly reasonable reconstruction of the object space. This is demonstrated in Example 4.

Example 4

An experimental setup to demonstrate the practical feasibility of the above technique is shown in Figure 5. The setup comprises prototype planar sensor array (on the far right), an impedance analyser and a host PC. The PC sends control signals to the analyser, which energises one excitation coil in the sensor array at a time, at a frequency of 100kHz. The voltage induced on a designated sensor coil is sent back to the analyser, which accurately computes an impedance and sends the result back to the PC. The excitation-sensor coil pair is switched manually and the

process is repeated for all coil-pairs and organised in a vector of measured impedances. First measurements are made with an empty object space. Next, two steel bars of diameter 25mm are placed in the object space, with centres at (-6.3, 3.7)cm and (6.3, 3.7)cm. The impedance vector is again measured, and the change in impedances are obtained by subtracting the empty-space values.

Figure 5: Experimental setup for Example 4.

The fractional impedance changes are then used to reconstruct the object space. The pixel-based algorithm is run for 1200 iterations and the resulting amplitude image is shown in Figure 6(a). The amplitude image clearly indicates the presence of two distinct objects, one over the rectangular window with corners (-7, 4)cm and (-5, 6)cm, and other over the window with corners (5, 4)cm and (7, 6)cm. The centres and radii of the objects are estimated to (-6.0, 4.9)cm, (5.9, 4.9)cm, 1.0cm and 0.9cm respectively. The parametric algorithm is initialised with theses values and after 10 iterations the parameters have converged as follows: one bar of diameter 25mm centred at (-6.1, 4.8)cm, and another of diameter 24mm centred at (5.8, 4.9)cm, as shown in Figure 6(b). While the radius and x-position of the scatterers have been closely reconstructed, the y-positions have been overestimated by about 1cm. This difference is mainly attributed to the fact that the prototype sensor array employs coils of circular cross-section, and their magnetic field penetrate less into the object space as compared to the two-dimensional model. The consequence is that scattering objects appear deeper than actual values.

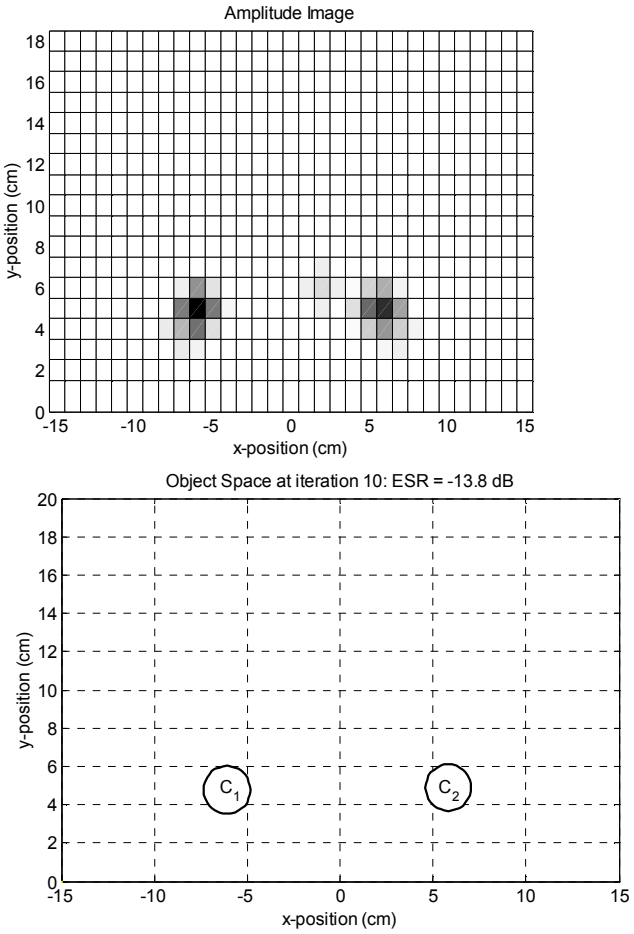

(a) (b)

Figure 6: (a) Amplitude image and (b) parametrically reconstructed object for Example 4.

CONCLUSION

In this paper, a method is presented for reconstructing the position and size of a number of scattering objects in a rectangular region of interest, from measurable data on the boundary of a region of interest. The method is a combination of two approaches: a pixel-based approach employing a linear reconstruction algorithm, namely SIRT, and a parametric approach using a modified version of the Levenberg-Marquardt algorithm. The first approach has the advantage of not assuming *a priori* information on the region of interest, and a simple linear model is used. An amplitude image is constructed from which essential information about the object space is obtained, such as number of objects, their approximate position and size. The results of the first approach are used as initialisation for the nonlinear parametric algorithm. The method is tested in several examples on both simulated and experimental data, and found to work satisfactorily.

REFERENCES

AL ZEIBAK, S., SAUNDERS, N.H. (1993). Feasibility study of in vivo electromagnetic imaging, *Phys. Med. Biol*., **38**, 151-160.

AULD, B.A., MUENNEMANN, F.G., RIAZIAT, M. (1984). Quantitative modelling of flaw responses in eddy current testing, *Research Techniques in Nondestructive Testing, 7*, 37-76.

BISSESSUR, Y., BHURTUN, C. (2005). Imaging of Steel Reinforcement Bars using Planar Electromagnetic Induction Tomography, In: *Proceedings of IEEE 3rd International Conference on Computational Cybernetics*, Mauritius, April 13-16, 255-258.

BISSESSUR, Y., PEYTON, A.J. (2004). Image Reconstruction from Impedance Change Measurements on a Prototype Planar EMT Sensor Array, In *Proc: 4th IATED Int. Conf. Visualisation, Imaging and Image Processing*, Marbella, Spain, 44-49.

BISSESSUR, Y., PEYTON, A.J. (2006). Computation of the forward and inverse problems in electromagnetic inductance tomography (EMT) for compact scattering objects, *International Journal of Information and Systems Sciences*, **2**(4), 557-574.
CIRIC, I.R., QIN, Y. (1997). Self-Adaptive Selection of the Regularisation Parameter for Electromagnetic Imaging, *IEEE Transactions on Magnetics*, **33**(2), 1556-1559.

COLTON, D., KRESS, R. (1998). *Inverse Acoustic and Electromagnetic Scattering Theory*, 2nd ed., Springer.

GAYDECKI, P.A., BURDEKIN, F. (1994). An inductive scanning system for two-dimensional imaging of reinforcing components in concrete structures, *Meas. Sci. Technol*. **5**, 1272-1280.

GILL, P.E., MURRAY, W., WRIGHT, M.H. (1981). *Practical Optimisation*, New York Academic.

ISAKSEN, Ø., NORDTVEDT, J.E. (1993). A new reconstruction algorithm for process tomography, *Meas. Sci. Technol*. **4**, 1464-1475.
PASTORINO, M. (1998). Short-Range Microwave Inverse Scattering Techniques for Image Reconstruction and Applications, *IEEE Trans. Inst. and Meas.,* **47**(6), 1419-1427.
PHAM, M.H., HUA, Y., GRAY, N. (2000). Imaging the solidification of molten metal by eddy currents – Part 1, *Inverse Problems*, **16**, 469-482.

PHAM, M.H., HUA, Y., GRAY, N. (2000). Imaging the solidification of molten metal by eddy currents – Part 2, *Inverse problems*, **16**, 483-494.

TAPP, H.S., PEYTON, A.J. (2003). A state of the art review of electromagnetic tomography, In *Proc: 3rd World Congress on Industrial Process Tomography*, ISBN 0 853 162409, Banff, Canada, 2-5 Sept. 2003, 340-346.

XIANDONG, M., PEYTON, A.J., BINNS, R., HIGSON, S.R. (2005) Electromagnetic Techniques for Imaging the Cross-Section Distribution for Molten Steel Flow in the Continuous Casting Nozzle, *IEEE Sensors Journal*, **5**(2), 224-232.